

Research Article

High-Precision Spotlight SAR Imaging with Joint Modified Fast Factorized Backprojection and Autofocus

Man Zhang,¹ Haolin Li,² and Guanyong Wang³ 

¹School of Electronics and Communication Engineering, Guangzhou University, Guangzhou 510006, China

²Institute of Spacecraft Application System Engineering, CAST, Beijing 100094, China

³Beijing Institute of Radio Measurement, Beijing 100854, China

Correspondence should be addressed to Guanyong Wang; gywang.sar@gmail.com

Received 16 March 2020; Revised 23 July 2020; Accepted 10 August 2020; Published 25 August 2020

Academic Editor: Francesco D'Agostino

Copyright © 2020 Man Zhang et al. This is an open access article distributed under the Creative Commons Attribution License, which permits unrestricted use, distribution, and reproduction in any medium, provided the original work is properly cited.

Fast factorized backprojection (FFBP) takes advantage of high accuracy of time-domain algorithms while also possessing high efficiency comparable with conventional frequency domain algorithms. When phase errors need to be compensated for high-resolution synthetic aperture radar (SAR) imaging, however, neither polar formatted subimages within FFBP flow nor the final Cartesian image formed by FFBP is suitable for phase gradient autofocus (PGA). This is because these kinds of images are not capable of providing PGA with a clear Fourier transform relationship (FTR) between image domain and range-compressed phase history domain. In this paper, we make some essential modifications to the original FFBP and present a scheme to incorporate overlapped-subaperture frame for an accurate PGA processing. The raw data collected by an airborne high-resolution spotlight SAR are used to demonstrate the performance of this algorithm.

1. Introduction

Backprojection (BP) is essentially a method of phased-array beamforming in the time domain. It is capable of handling an arbitrary flight path and producing synthetic aperture radar (SAR) images free of geometric distortions and defocus effects [1]. Despite of these advantages, the direct BP algorithm is still difficult to put in practice due to its low efficiency. Some studies about polar formatting method for spotlight-mode SAR imaging are conducted to improve the computational efficiency [2]. During the past decade, a number of fast BP algorithms [3–7] for accelerating BP integral have been proposed, and fast factorized BP (FFBP) is the most representative. Based on recursive partitioning, FFBP consists of a series of stages. A major characteristic of FFBP is that subaperture length increases successively, whereas the beam spacing decreases. Finer angular resolution subimages are formed in local polar coordinates by combining

coarse subimages from the previous stage. With high accuracy and efficiency, FFBP takes the best from both time and frequency domain algorithms. Therefore, SAR imaging via FFBP has been attracting more and more attention in recent years.

During airborne SAR imaging, air turbulence inevitability induces platform deviation from ideal trajectory. However, it is noteworthy that even the most sophisticated motion measurement system may be not sufficient to ensure diffraction-limited SAR images. Therefore, autofocus techniques are required for further processing, which is studied in [8], but research studies about autofocus combined with BP or FFBP are not comprehensive. Different from the methods based on varying antenna path parameters [9] and maximizing image sharpness [10–13], our primary aim is to achieve an accurate autofocus processing within FFBP by using current autofocus techniques, such as mapdrift (MD) autofocus, minimum-entropy autofocus, and phase gradient

autofocus (PGA). In [14], basic theories about the use of autofocus were developed and a scheme of incorporating multiple aperture mapdrift (MAMD) autofocus into FFBP was presented. As a promising start, we firmly believe FFBP is capable of working with other autofocus techniques and can be extended to satisfy our growing need in much more complex scenarios. Generally, phase errors are predominantly low-order phase errors introduced by deviation from ideal trajectory, while mechanical vibration and random propagation will inevitably induce high-order phase errors [15]. However, MAMD and other parametric model-based algorithms all predefine a low-order explicit expression for phase errors and neglect the high-order components. In contrast, PGA has been verified to be a robust technique and is being widely used throughout the SAR community [16]. As a nonparametric algorithm, PGA imposes no restriction on the form of phase errors, so it can achieve excellent restorations under more general conditions. However, directly incorporating PGA into the time-domain algorithms is not easy. To our best knowledge, [17] is the only work considering that PGA is used to refocus SAR images formed by the direct BP. As revealed in [18], there are some significant factors which should be taken into account. Firstly, the spread of azimuth impulse response function (IRF) do not lie in the horizontal dimension of a backprojected image. Secondly, the Fourier transform relationship (FTR) between the image and its corresponding range-compressed phase history is not sufficiently explicit for a backprojected image.

In this paper, we propose a scheme to incorporate PGA into FFBP and achieve accurate autofocus processing for high-resolution spotlight SAR imaging. The main contributions of this work are twofold:

- (1) Pseudopolar coordinate system is employed as the imaging plane, and an analytic expression for azimuth IRF in a backprojected image is derived. Actually, a line-of-sight (LOS) pseudopolar coordinate system not only ensures the spread of azimuth IRF along the horizontal dimension but also provides an approximate FTR for the use of PGA.
- (2) Subaperture phase errors estimated by PGA cannot be directly applied to correct the range-compressed phase history data, otherwise they will cause relative shifts among subimages. To achieve an accurate phase correction, overlapped-subaperture frame (OSF) is introduced into FFBP to obtain a full-aperture phase error by coherently combining subaperture phase errors. As phase correction is recursively performed, phase estimation tends to converge and the degraded image becomes refocused.

2. Modified FFBP for Focusing Spotlight SAR Data

In the original FFBP, both polar formatted subimages and the final Cartesian image are formed, but neither of them

can provide PGA with a FTR between image domain and range-compressed phase history domain. In order to establish a FTR, we focus on theoretical analysis and make some significant modifications to the original FFBP in this section.

2.1. Azimuth IRF in the Pseudopolar Coordinate System. An ideal imaging geometry of spotlight SAR is shown in Figure 1; the model is based on the assumption of flat land. The platform moves along the x -axis with velocity v and generates a synthetic aperture of length L . During the data acquisition, the sensor continuously steers its antenna beam onto the scene center C . Taking the aperture center O as the origin of the polar coordinate system, the coordinates of point target P is (r_p, θ_p) , where r_p is the range measured from O to P and θ_p is the bearing angle measured away from the broadside direction. For the sake of clarity, we define a pseudopolar coordinate system described by r and Θ , where Θ is the sine value of θ , namely, $\Theta = \sin \theta$. The slant range from the sensor to target P is given by

$$R(r_p, \Theta_p; X) = \sqrt{r_p^2 + X^2 - 2r_p X \Theta_p}, \quad -\frac{L}{2} \leq X < \frac{L}{2}, \quad (1)$$

where X is aperture position and Θ_p is equal to $\sin \theta_p$.

The sensor transmits linear frequency-modulated (LFM) signal with bandwidth B and carrier frequency f_c . Considering target P with a unit reflectivity coefficient, the baseband signal after range compression is expressed as

$$s_{MF}(\tau; X) = W_a(X) \sin c [B(\tau - \tau_p)] \exp(-j2\pi f_c \tau_p), \quad (2)$$

where τ is the fast time, W_a represents a common antenna pattern, and $\tau_p = 2R(r_p, \Theta_p; X)/c$ corresponds to the round-way time delay. Equation (2) ignores antenna gain and $1/R^2$ propagation decay factor in the amplitude term.

BP is essentially an integral process performed in the time domain. For a given aperture position X_0 , $s_{MF}(\tau; X_0)$ needs to be backprojected to every pixel in the desired imaging grid, and each pixel is assigned a value according to the time delay corresponding to the range between the sensor and the pixel; for all available aperture positions, BP integral is achieved by coherent accumulation along the range history of each pixel. Importantly, an enormous advantage of BP is that it allows for image reconstruction onto an arbitrary imaging grid. In [10, 17], a range and sine of the bearing angle grid is employed as an imaging plane. In this paper, we also adopt this imaging grid and name it pseudopolar coordinate system.

Due to the limited Doppler bandwidth of spotlight SAR, azimuth IRF cannot be a Dirac function which is just located at one angular cell. For target P , the peak of its azimuth IRF is concentrated at the Θ_p angular cell and the side lobes spread out in the azimuth direction at the r_p range cell. Without loss of generality, the contribution of target P to a pixel located at (r_p, Θ) in the pseudopolar coordinate system is given by

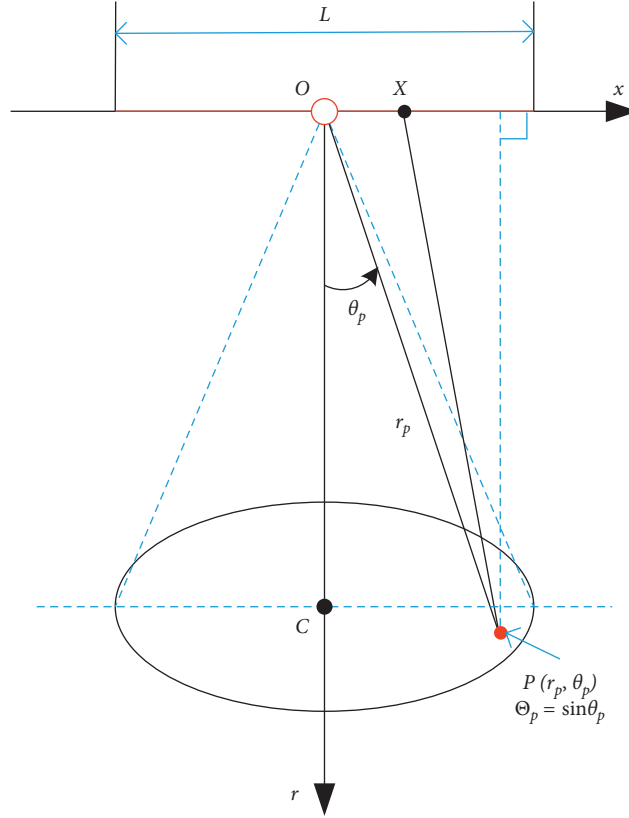


FIGURE 1: Imaging geometry for spotlight SAR in polar coordinates.

$$\begin{aligned}
 h(r_p, \Theta) &= \int_{-\infty}^{+\infty} s_{MF} \left[\tau = \frac{2R(r_p, \Theta_p; X)}{c}; X \right] \exp \left[j \frac{4\pi}{\lambda} R(r_p, \Theta; X) \right] dX \\
 &= \int_{-\infty}^{+\infty} W_a(X) \text{sinc}(0) \exp \left[-j 2\pi f_c \frac{2R(r_p, \Theta_p; X)}{c} \right] \\
 &\quad \cdot \exp \left[j \frac{4\pi}{\lambda} R(r_p, \Theta; X) \right] dX \\
 &\approx \int_{-(L/2)}^{(L/2)} \exp \left[-j \frac{4\pi}{\lambda} R(r_p, \Theta_p; X) \right] \exp \left[j \frac{4\pi}{\lambda} R(r_p, \Theta; X) \right] dX \\
 &= \int_{-(L/2)}^{(L/2)} \exp \left[-j \frac{4\pi}{\lambda} \Delta R(r_p, \Theta; X) \right] dX,
 \end{aligned} \tag{3}$$

where $\Delta R(r_p, \Theta; X) = R(r_p, \Theta_p; X) - R(r_p, \Theta; X)$ is the differential range between $R(r_p, \Theta_p; X)$ and $R(r_p, \Theta; X)$.

During the derivation of equation (3), we introduce a general approximation that antenna pattern $W_a(X)$ is modeled as a rectangular window function, i.e., $\text{rect}(X/L) = \begin{cases} 1 & -(L/2) \leq X < (L/2) \\ 0 & \text{elsewhere} \end{cases}$. It should be emphasized that $h(r_p, \Theta)$ is not an image as normally formed by BP integral, but an impulse response for the pixels located at the r_p range bin. When $\Theta = \Theta_p$, the main lobe of the azimuth IRF is located at the Θ_p angular cell. Despite all that it is not hard to explain the relationship between a reconstructed image and its pixels. Given impulse responses for all

the pixels, theoretically, the image could be reached by $I(r, \Theta) = \sum_r \sum_{\Theta} h(r, \Theta)$.

To derive an analytic expression of azimuth IRF, $\Delta R(r_p, \Theta; X)$ is extended into the third-order Taylor series, i.e.,

$$\begin{aligned}
 \Delta R(X; r_p, \Theta) &= R(X; r_p, \Theta_p) - R(X; r_p, \Theta) \\
 &\approx (\Theta - \Theta_p)X + \frac{\Theta^2 - \Theta_p^2}{2r_p} X^2 \\
 &\quad + \frac{(\Theta - \Theta_p)(\Theta^2 + \Theta_p\Theta + \Theta_p^2 - 1)}{2r_p^2} X^3.
 \end{aligned} \tag{4}$$

By neglecting the X^2 and other higher-order terms in $\Delta R(r_p, \Theta; X)$, we can rewrite equation (3) and obtain a compact expression, which is given by

$$\begin{aligned}
 h(r_p, \Theta) &\approx \int_{-(L/2)}^{(L/2)} \exp \left[-j \frac{4\pi(\Theta - \Theta_p)}{\lambda} X \right] dX \\
 &= \int_{-(L/2)}^{(L/2)} \exp(-jK_{\Theta}X) dX = h(r_p, K_{\Theta}),
 \end{aligned} \tag{5}$$

where K_{Θ} represents angular wavenumber. In equation (5), a generalized Fourier transform is approximately developed between K_{Θ} and X . It states that the azimuth impulse

response along X in the r_p range bin is achieved by the Fourier transform of the range-compressed data, which is critical to the use of autofocus techniques.

In the following, we analyze the constraint which needs to be fulfilled for the validity of equation (5). In [14], it assumes that the majority of energy of azimuth IRF is concentrated with a small region size corresponding to the angular resolution $\Delta\Theta = \lambda/2L$. The contributions of higher-order terms take minimal effect on the BP integral if quadratic phase error (QPE) induced by X^2 term is less than $\pi/16$ in the neighborhood of Θ_p , namely, $\Theta \in [\Theta_p - \Delta\Theta, \Theta_p + \Delta\Theta]$. Noting that $\Delta\Theta$ keeps positive, we can determine QPE as follows:

$$\text{QPE} = \frac{4\pi}{\lambda} \frac{\Theta^2 - \Theta_p^2}{2r_p} X^2 \leq \frac{4\pi}{\lambda} \frac{\Delta\Theta \cdot (2|\Theta_p| + \Delta\Theta)}{2r_p} X^2 \leq \frac{\pi}{16}. \quad (6)$$

By simplifying equation (6), we can obtain

$$8L \cdot |\Theta_p| + 2\lambda \leq r_p. \quad (7)$$

As equation (7) is the constraint of equation (5), if the pixel close to the edge of the imaging grid can satisfy equation (7), all the pixels on this grid can meet this constraint, too. Therefore, the final constraint is given by

$$8L \cdot \Theta_{\max} + 2\lambda \leq r_{\min}, \quad (8)$$

where Θ_{\max} is the maximum value of Θ and r_{\min} is the minimum value of r .

For spotlight SAR, the angular range of pseudopolar coordinates satisfies $|\Theta| \leq \sin(\theta_{\text{BW}}/2)$, where θ_{BW} is antenna azimuth beamwidth. In this case, equation (8) can be straightforwardly written as

$$8L \cdot \sin\left(\frac{\theta_{\text{BW}}}{2}\right) + 2\lambda \leq r_{\min}. \quad (9)$$

For the sake of clarity, let us take the X-band spotlight SAR used in the experiments in Section 4 as an example, where $L = 1.17$ km, $r_{\min} = 10.1$ km, and $\theta_{\text{BW}} \approx 6.78$ degrees. By substituting these parameters into equation (9), $8L \cdot \sin(\theta_{\text{BW}}/2) + 2\lambda \approx 553.72$ m is less than r_{\min} , which satisfies the constraint of equation (9). Therefore, the approximation of equation (5) keeps valid and is precise enough to ensure the validity of FTR. Besides, wavelength λ is relatively small compared with L and r_{\min} , which can be removed from equations (8) and (9).

2.2. The Modified FFBP Algorithm. Original FFBP splits up BP integral into an infinite sum over finite subapertures, so reconstructing each subimage can be considered as an individual direct BP. Motivated by Section 2.1, we can introduce the pseudopolar coordinate system into the original FFBP instead of the polar coordinate system and refer to this new algorithm as the modified FFBP.

Based on aperture factorization and recursive fusion, FFBP consists of a series of stages. Assume that there are K subapertures in the g th stage, where $g = 1, 2, \dots, G$ and G is the total number of stages. K subapertures generate K subimages. Each subimage is created onto a local polar grid with the origin located at its corresponding subaperture center. Noting the differences among these subimages, we use $(r, \Theta_k^{(g)})$ to describe the k th polar grid in the g th stage. According to Section 2.1, the k th subimage $I_k^{(g)}$ can be expressed as

$$I_k^{(g)}(r, K_{\Theta_k^{(g)}}) = \sum_r \sum_{\Theta_k^{(g)}} h(r, \Theta_k^{(g)}), \quad (10)$$

where $K_{\Theta_k^{(g)}}$ represents the angular wavenumber corresponding to the k th subaperture.

Based on the definition of Doppler f_a , $K_{\Theta_k^{(g)}}$ is in proportion to f_a with a scale factor of $2\pi/v$. In this sense, azimuth focusing of $I_k^{(g)}$ is performed in the Doppler domain, which is equivalent to the azimuth focusing domain of SPECAN imaging [18]. Although the modified FFBP implements BP integral in the time domain, by using pseudopolar coordinates, subimages could be considered as range-Doppler images. Moreover, an implied demand of autofocus is that the spread of azimuth IRF should be along the horizontal dimension of an image. The solution to this problem is simple, but it is not categorically stated in [4, 5]. By learning experience from polar format algorithm (PFA), we find that LOS polar interpolation can rotate the orientation of the imaged scene while keeping the spread of azimuth IRF along the horizontal dimension [15]. In this paper, all local pseudopolar coordinates in the modified FFBP are established along the direction of the LOS from each subaperture center to the scene center. In this way, we can obtain nonsquinted data spectrum and ensure the orthogonality between its range and azimuth dimension so that we can keep the azimuth IRF spreading out in the azimuth direction. Figure 2 shows the last two subimages of the modified FFBP. Figures 2(a) and 2(b) represent exactly the same scenes (five point targets arranged in a cross line) and correspond to the last two subapertures. Because of LOS coordinates, the imaged scenes are rotated through a slight angle in opposite directions as the red dashed lines outline. However, it will be found that the spread of azimuth impulse response for all targets lies in the horizontal dimension.

It should be noted that the LOS polar grid used in the modified FFBP is a polar grid in the image domain, while PFA uses a polar grid in the frequency domain. The modified FFBP inherently accommodates wavefront curvature and elevation-induced defocus effects arising from out-of-plane motion of platform [17]. Therefore, the modified FFBP is capable of producing SAR images without geometric distortions and defocus effects. By contrast, PFA has a limited depth of focus. If we attempt to produce distortion-free SAR image by using PFA,

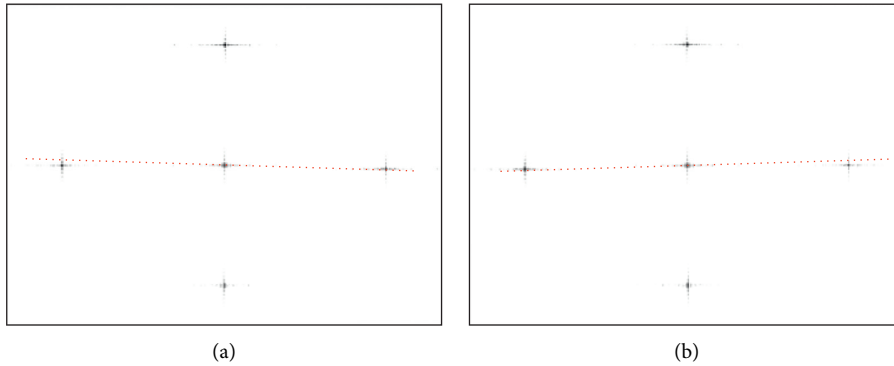


FIGURE 2: The last two subimages reconstructed by modified FFBP. (a) Subimage 1. (b) Subimage 2.

several postprocessing corrections need to be applied [15].

3. Overlapped-Subaperture Frames and PGA Processing

FTR is what we emphasize in this paper, but it is not an inference for time-domain algorithms after all. In Section 2, we make some necessary modifications to the original FFBP by introducing LOS pseudopolar coordinates. Noting that all the subimages created by the modified FFBP can satisfy the FTR requirement of PGA, we are able to employ PGA to extract subaperture phase errors from subimages. However, here emerges another issue: subaperture phase errors cannot be directly used to refocus the degraded subimages, otherwise they will cause relative shifts among the subimages. This fact arises for the reason that the linear component of a subaperture phase error has been removed by “circular shifting” operation [16]. Therefore, it is necessary to retrieve the linear component belonging to each subaperture phase error before phase correction. How to achieve this goal is the main topic of this section.

In [19], overlapped-subaperture frame (OSF) is introduced to build a bridge connecting original subaperture phase errors and a full-aperture phase error. Each desired subaperture phase error can be updated with its linear component according to the full-aperture phase error function. Enlightened by this thought, this section includes two parts: building OSF and implementing PGA processing within the recursion of the modified FFBP.

3.1. Overlapped-Subaperture Frames. Overlapped-subaperture technology was first combined with PFA to correct spatially-variant phase errors in spotlight SAR imaging [20]. Since then, it has been widely used to recover continuous full-aperture phase errors or estimate range-dependent phase errors in wide-swath stripmap SAR. Compared with the manner of building overlapped subapertures in [20], the modified FFBP should take a little more specific details into consideration. For a clear interpretation, a counter example that the once-through designed OSF fails our need is first given as follows.

In the first stage of the modified FFBP, the whole aperture is divided into several overlapped subapertures. Assuming that each subaperture contains $2N$ samples and the overlap ratio is $(1/2)$, there should be N overlapped samples between two adjacent subapertures. In the second stage, each new subaperture will contain $2 \times 2N - N = 3N$ samples after aperture fusion. Because the number of the samples shared by two adjacent subapertures remains N , and the overlap ratio is $1/3$ at this time. As the processing goes on, the length of subaperture increases, but the overlap ratio keeps descending, which is unfavorable to a coherent combination of subaperture phase errors.

To recover a reliable full-aperture phase error function, obviously, we need to guarantee that the overlap ratio of two adjacent subapertures is big enough. In the following, we will present an innovative method of founding OSF within the modified FFBP. To illustrate this method, here we take a four-step processing as an example for analysis, and its critical steps are as follows:

Step 1: like the original FFBP, the modified FFBP performs the identical processing until 8 non-overlapped subapertures are left, and each one contains N samples. This condition is described as the first row (from top to bottom) in Figure 3(a), where the blue line segment represents subaperture and the red circle denotes subaperture center.

Step 2: perform aperture fusion among any two adjacent subapertures, and then 7 subapertures can be formed from 8 previous subapertures. As a consequence, the subaperture length is extended to $2N$ and the overlap ratio is $1/2$. Compared with the second row in Figure 3(a), the red line segments in the second row in Figure 3(b) are newly formed by OSF.

Step 3: employ PGA to extract subaperture phase errors from the 7 subimages formed by Step 2, and the detailed description will be given in the next section. It should be emphasized that, of the 7 new subapertures, only the odd ones, namely, 4 nonoverlapped subapertures will be transported to the next stage for aperture fusion, which are shown as the blue line segments in the second row of Figure 3(b). The other 3 subapertures shown as the red ones will be directly deleted after phase estimation.

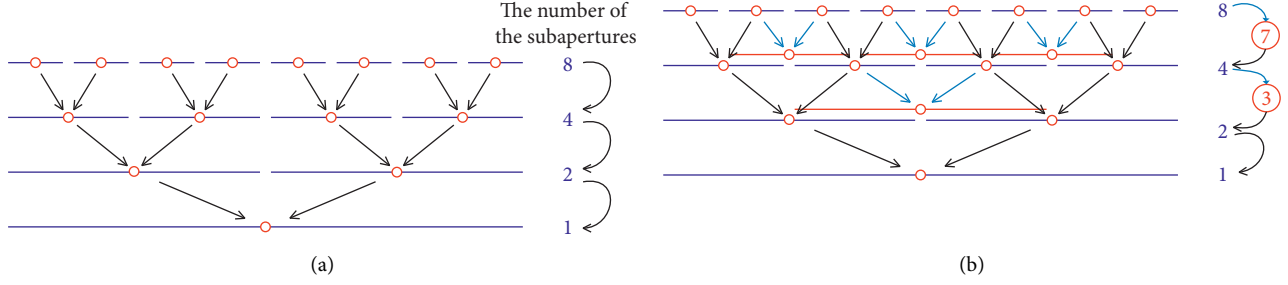


FIGURE 3: Change of the subapertures in the last four stages. (a) The original FFBP. (b) OSF in the modified FFBP.

Step 4: repeat Steps 2~3 and then the last two subapertures are generated. In this situation, there is no need to build OSF, but should carry out the same processing as the original FFBP does in the last stage.

An advantage of this method is that the overlap ratio being 1/2 keeps unchanged in spite of different subaperture lengths at different stages. OSF for phase correction is not required in a stage-by-stage manner for the reason that PGA is instinctively a recursive process. Therefore, building OSF in two or three successive stages is enough for practical use.

3.2. PGA Processing. “Original subaperture phase errors—Full-aperture phase error—Desired subaperture phase errors” is a direct way to achieve an effective phase correction. Designed to obtain a reliable full-aperture phase error, OSF is an essential link in this chain. With LOS pseudopolar coordinates and OSF, preparations for PGA processing are all complete.

Assume that phase correction is not performed in the modified FFBP until the g th stage. Assuming the influence of phase errors becomes obvious on degrading image quality in this stage, we need to build OSF and perform an effective PGA processing. Assume that there are K subapertures in the beginning of g th stage. According to Section 3.1, K subapertures can generate $K - 1$ overlapped subapertures with the overlap ratio being 1/2 and each subaperture corresponds a single subimage. Based on the FTR derived in Section 2, the range-compressed phase history of $I_k^{(g)}$ is given by

$$H_k^{(g)}(r, X_k^{(g)}) = \int I_k^{(g)}(r, K_{\Theta_k^{(g)}}) \exp[jK_{\Theta_k^{(g)}} \cdot X_k^{(g)}] dK_{\Theta_k^{(g)}}, \quad (11)$$

where $K_{\Theta_k^{(g)}}$ and $X_k^{(g)}$ correspond the horizontal coordinate axis of image domain and range-compressed phase history domain, respectively, B_d is the Doppler bandwidth, and $f_0^{(k)}$ denotes the Doppler centroid of the k th subaperture. Equation (11) is a Fourier transform of $I_k^{(g)}$ from image domain to range-compressed phase history domain, so we can obtain the phase history of point in range-compressed phase history domain. The value range limitation of $K_{\Theta_k^{(g)}}$ is given by

$$K_{\Theta_k^{(g)}} \in \left[\frac{2\pi}{v} \left(f_0^{(k)} - \frac{B_d}{2} \right), \frac{2\pi}{v} \left(f_0^{(k)} + \frac{B_d}{2} \right) \right], \quad k \in [1, K - 1]. \quad (12)$$

Supposing the bulk of motion errors have been effectively corrected by the high-precision motion measurement system, such as global positioning system (GPS) and/or inertial navigation unit (IMU), migration caused by the residual errors is less than one range cell. In this section, the sign ϕ_k denotes the phase error retained in the real range-compressed phase history $H_k^{(g)}$, and $\phi_k^{(g)}$ is a function of subaperture position $X_k^{(g)}$. Therefore, the relationship between the theoretical value $H_k^{(g)}$ and the real value $H_k^{(g)}$ could be described as

$$H_k^{(g)}(r, X_k^{(g)}) = H_k^{(g)}(r, X_k^{(g)}) \exp[-j\phi_k^{(g)}(X_k^{(g)})]. \quad (13)$$

Based on equation (13), we can employ PGA [16] or weight PGA (WPGA) [21] to extract subaperture phase error from $H_k^{(g)}$. As a derivative of PGA, WPGA utilizes the signal-to-clutter ratio (SCR) to compute the weights of range cells. Large weights are applied to range cells with high SCRs. Assume that WPGA has been employed to each subimage, and the estimated subaperture phase errors are denoted by $\hat{\phi}_1^{(g)}, \hat{\phi}_2^{(g)}, \dots, \hat{\phi}_{K-1}^{(g)}$, where “ $\hat{}$ ” represents the estimated value of a variable. Compared with the real values, the most difference of these $K - 1$ estimated values is that the linear components reflecting the interrelation of subapertures have been removed by “circular shifting” operation in WPGA. According to the previous analysis, we need to update each subaperture phase error with its linear phase from a full-aperture phase error function.

To recover a full-aperture phase error function, subaperture phase estimates are coherently combined by eliminating the unknown linear difference between the phase errors extracted from the overlapped samples of the neighboring subapertures, which are illustrated in Figure 4. In practice, the subaperture phase estimates fluctuate sharply and the precision degrades with the increase of clutter and high frequency noise. For a smooth full-aperture phase error function, the phase filter is usually required. After a coherent combination and a smooth filtering, the full-aperture phase error function $\hat{\phi}^{(g)}(X)$ is recovered. Noting that each subaperture has a definite subaperture span $X^{(k)}$, $k = 1, 2, \dots, K - 1$, we can recalculate subaperture phase errors from $\hat{\phi}^{(g)}(X)$. Of these $K - 1$ subimages, the

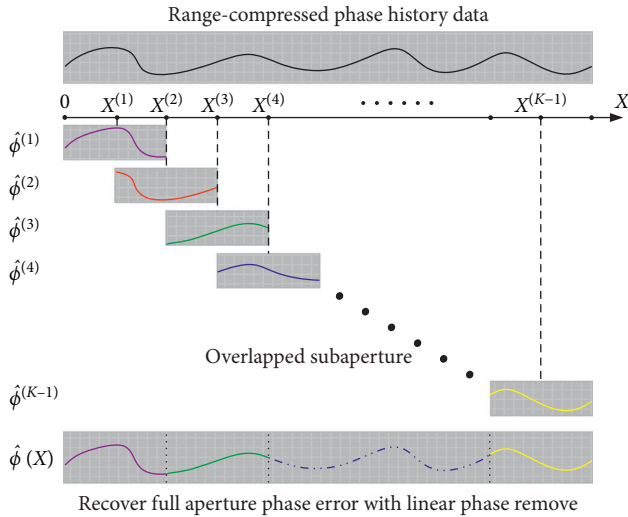


FIGURE 4: Full-aperture phase error combination.

even ones (totally $(K/2) - 1$) are no longer needed after phase estimation and deleted from memory, and the other $K/2$ subimages should be refocused before they are transported to the $g + 1$ th stage. So, we perform motion compensation to these $K/2$ subimages with desired subaperture phase errors, including residual range cell migration (RCM) correction and phase error removal. Until now, we complete all PGA processing in the g th stage. The detailed illustration is shown in Figure 5. If it is necessary to perform phase error correction in the $g + 1$ th stage, we just repeat the operations mentioned above.

Profit from OSF scheme, PGA processing can be performed in a recursive manner and compatibly blended into the modified FFBP. Undoubtedly, OSF introduces computational burden, but only two or three successive stages are enough for PGA to refocus a full-resolution image up to an acceptable level. It can be regarded as a tradeoff between the image quality and the processing efficiency. Moreover, the “windowing” step of PGA in this paper should be emphasized that the maximum window width becomes small after the first applying PGA, which is of benefit to the rapid convergence of phase estimation.

4. Experiments

In this section, the raw data collected by an airborne high-resolution spotlight SAR are used to demonstrate the performance of this algorithm. The main parameters of the SAR system are tabulated in Table 1. In the experiment, the synthetic aperture time is 7.8 seconds and each pulse contains 8192 range bins. The image is $0.8\text{ km} \times 1.2\text{ km}$ in size with range and azimuth resolutions of $0.15\text{ m} \times 0.15\text{ m}$ (angular resolution varies in the range direction and 0.15 m is the resolution corresponding to the closest slant range). Empirically, when the number of samples is 2048 in each subaperture, angular resolution is 1.2 m and the influence of phase errors emerges gradually. Then, we begin to build OSF and perform PGA processing to coarse subimages. Although phase correction has

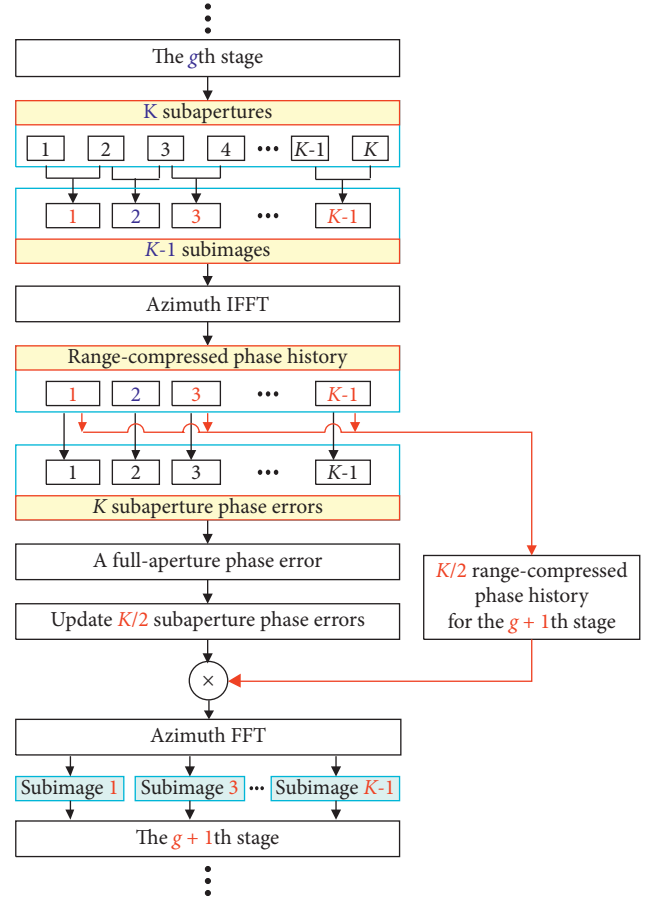


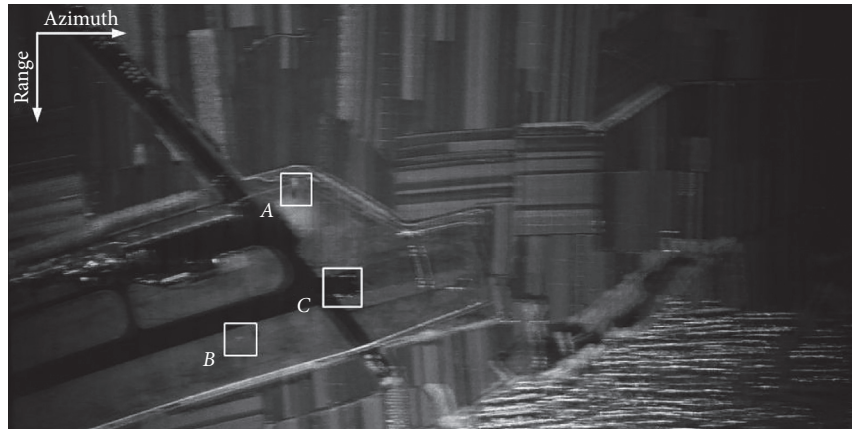
FIGURE 5: Block diagram of OSF in the modified FFBP.

been performed in the current stage, fractional phase errors may still exist in subimages. Due to the fact that angular resolution increases to 0.6 m in the next stage, the influence of residual errors will be magnified. Therefore, we also need to perform PGA processing to correct residual errors in the next stage. On the contrary, the signal-to-noise ratio of the subimages will be higher as the subaperture becomes longer, which also enhances the performance of PGA.

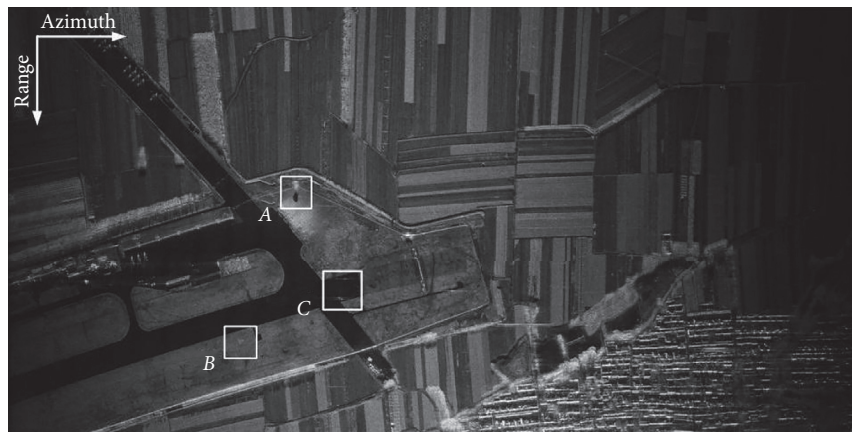
The processed results and estimated motion error are presented in Figure 6. Due to the existence of motion errors, Figure 6(a) without autofocus involves in serious image blurs, while Figure 6(b) processed by the proposed method is well-focused over the whole scene. Radial motion error estimated by WGPA is observed in Figure 6(c). In order to assess the performance of the algorithm, subscenes A–C from Figure 6 are magnified in Figure 7. For each pair of subscene images in Figure 6, the upper blurred image is extracted from Figure 6(a), while the lower one is obtained by the proposed method. Obviously, all subscene images in Figure 7 generated by the proposed method are well-focused, such as the shadow of the tree and the corner reflector array aligned in “T” form. In Scene C, two close-located corner reflectors outlined by circle “1” are arranged with 0.15 m distance in azimuth, and another two outlined by circle “2” are placed with 0.15 m distance in range. To demonstrate the performance of the proposed method, we give imaging

TABLE 1: Main parameters of the SAR system.

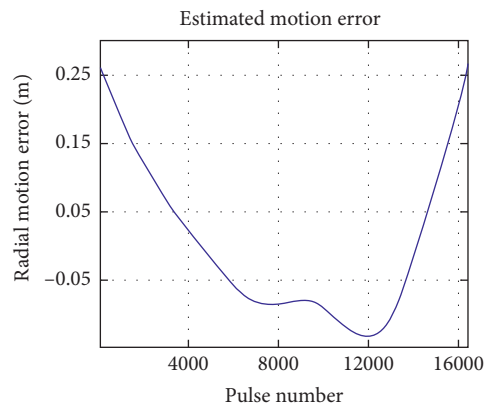
Wave band	Transmitted bandwidth	Pulse repetition frequency	Closest slant range	Pulse number
X-band	1.16	2100	10.5	16384



(a)



(b)



(c)

FIGURE 6: Images formed by the modified FFBP. (a) Uncompensated SAR image; (b) SAR image restored by PGA; (c) radial error extracted from phase error by PGA.

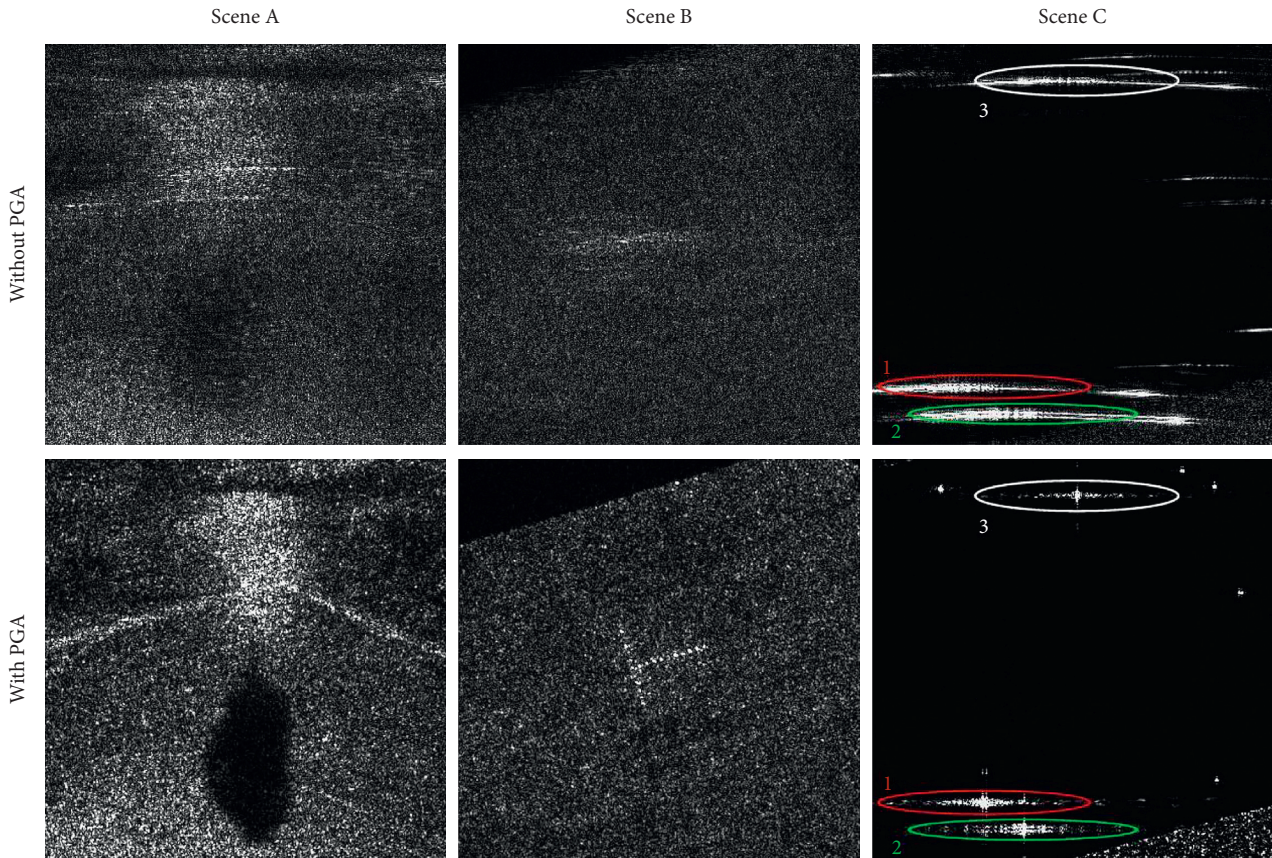


FIGURE 7: Magnified images of subscenes A–C in Figure 6.

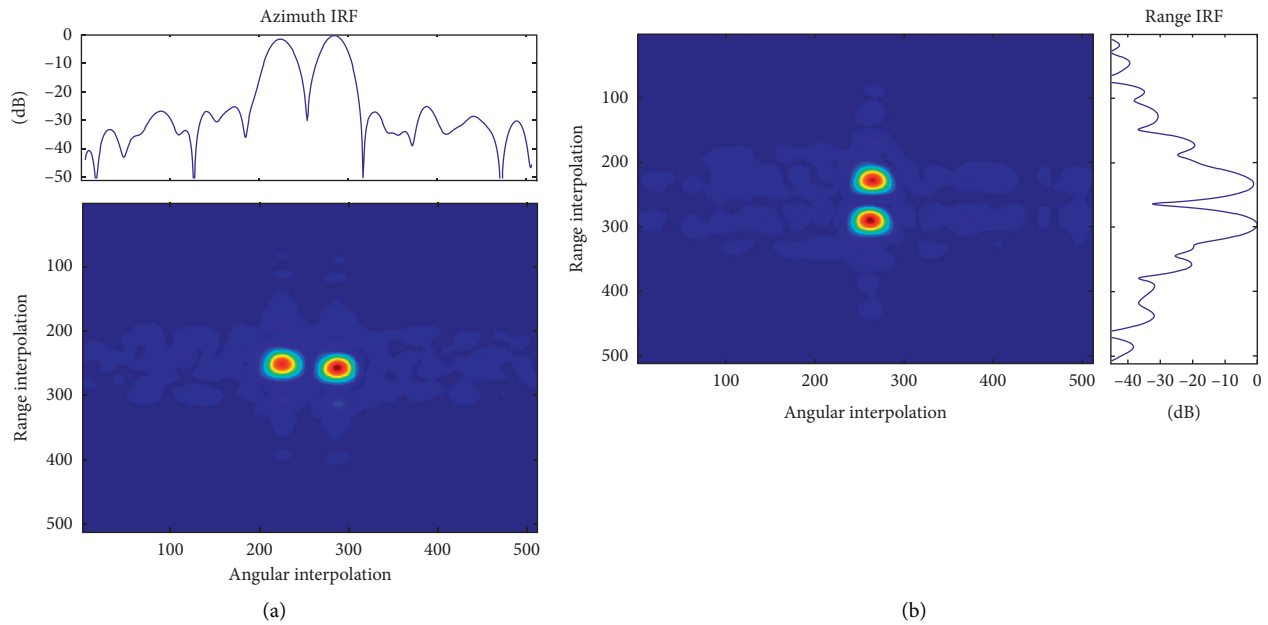


FIGURE 8: Images and IRFs. (a) Imaging result and azimuth IRF of the reflector in circle “1”; (b) imaging result and range IRF of the reflector in circle “2.”

results and two-dimensional IRFs with hamming windowing in Figure 8, where one can clearly find that the depth of notch between the two peaks is lower than -30 dB and the

side lobes of IRFs are almost below -20 dB. This fact provides a clear evidence to show the great discrimination of our proposed method. To evaluate the image quality, both range

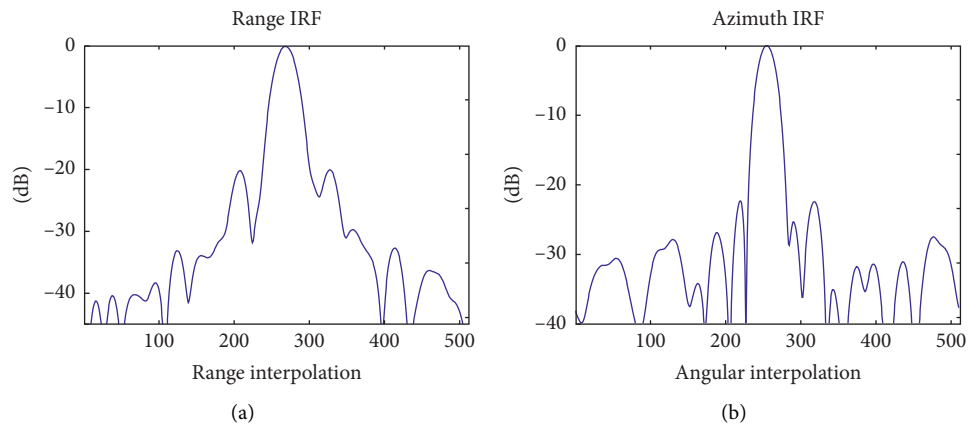


FIGURE 9: Two-dimensional IRFs of the reflector in Scene 3. (a) Range IRF. (b) Azimuth IRF.

TABLE 2: Main parameters of the SAR system.

Wave band	Transmitted bandwidth (GHz)	Pulse repetition frequency (Hz)	Closest slant range (km)	Pulse number
Ku-band	500	2000	5	8192

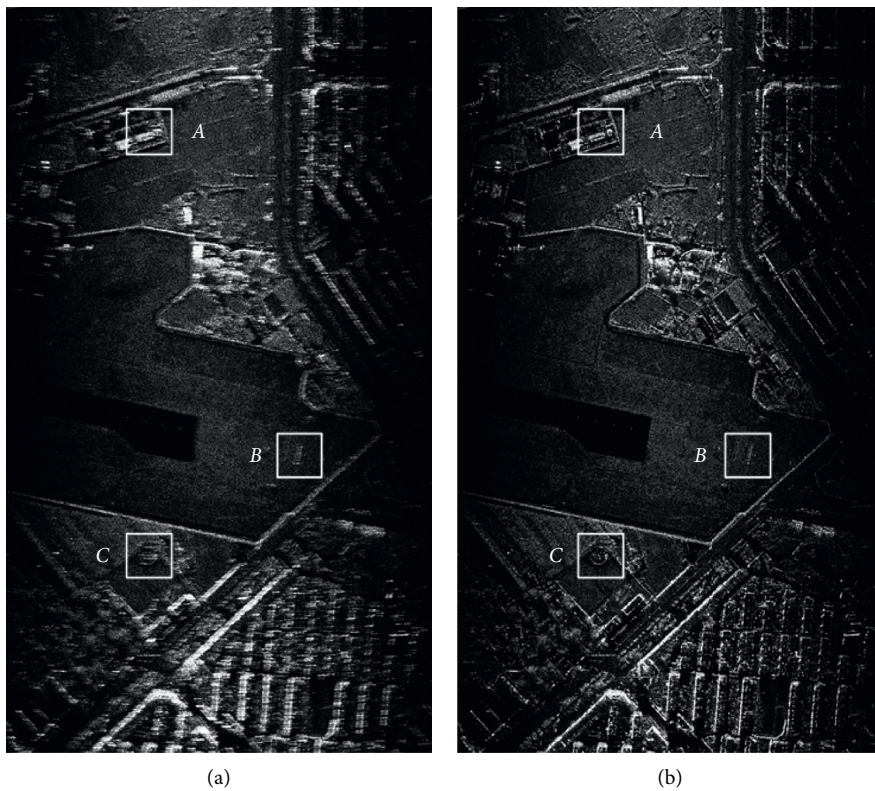


FIGURE 10: Continued.

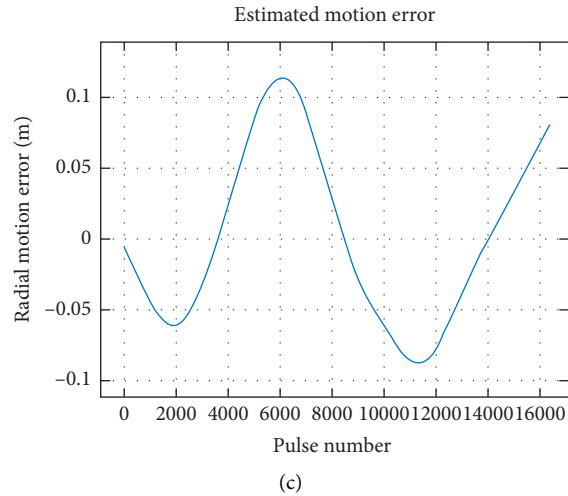


FIGURE 10: Images formed by the modified FFBP. (a) Uncompensated SAR image; (b) SAR image restored by PGA; (c) radial error extracted from phase error by PGA.

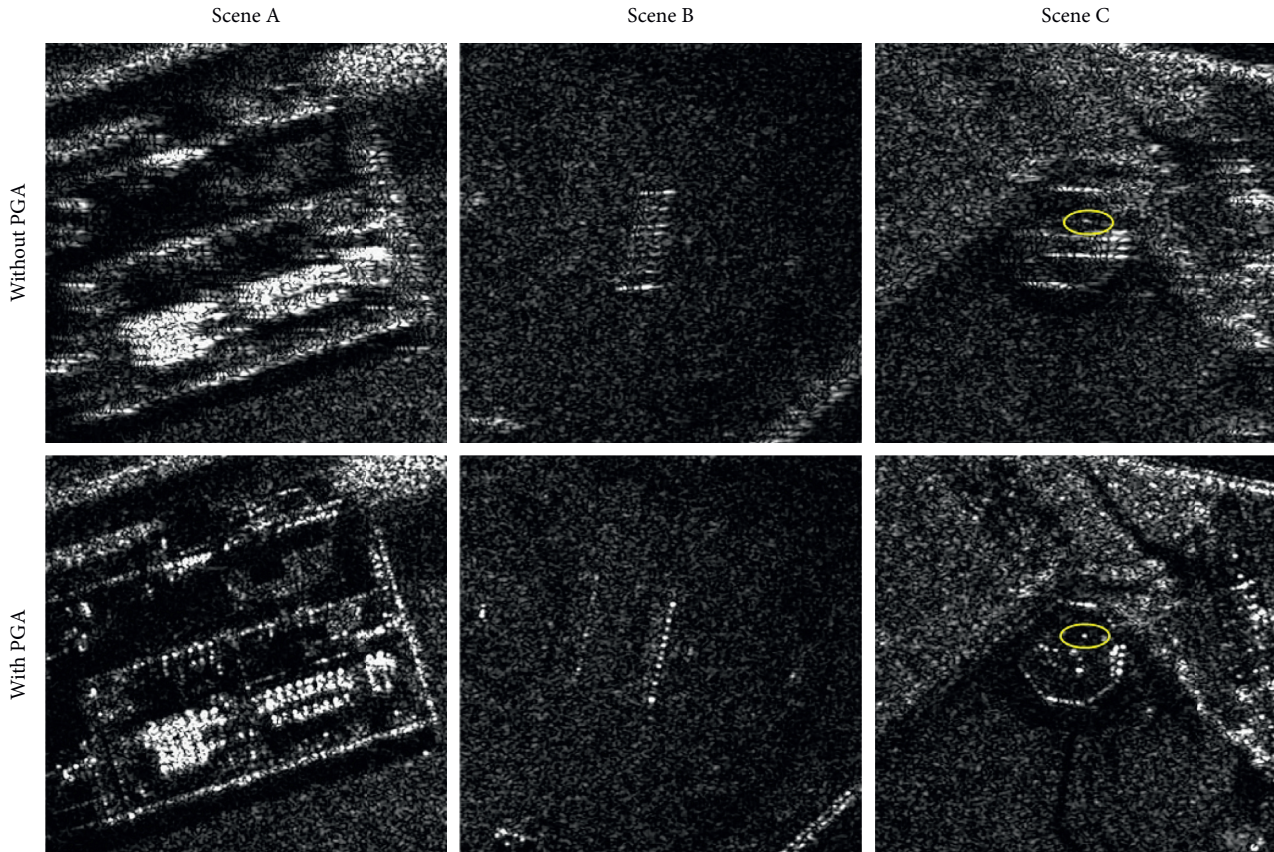


FIGURE 11: Magnified images of subscenes A–C in Figure 10.

and azimuth IRFs of a single reflector outlined by circle “3” are given in Figure 9. The level of side lobes below -20 dB also gives us a compelling reason to believe the effectiveness of our proposed method.

From Figure 6(c), the radial error is larger than one range resolution cell, which is beyond the assumption that migration caused by the residual errors should be usually less

than one range cell. Fortunately, RCM can be corrected in the range frequency domain during FFBP imaging. Through the results above, this skill has succeeded in image processing and RCM correction. It makes us to believe that some other skills or ideas in frequency domain algorithms may be adopted in the modified FFBP, such as the correction of range-dependent phase errors in wide-swath SAR images [22]. Another set of

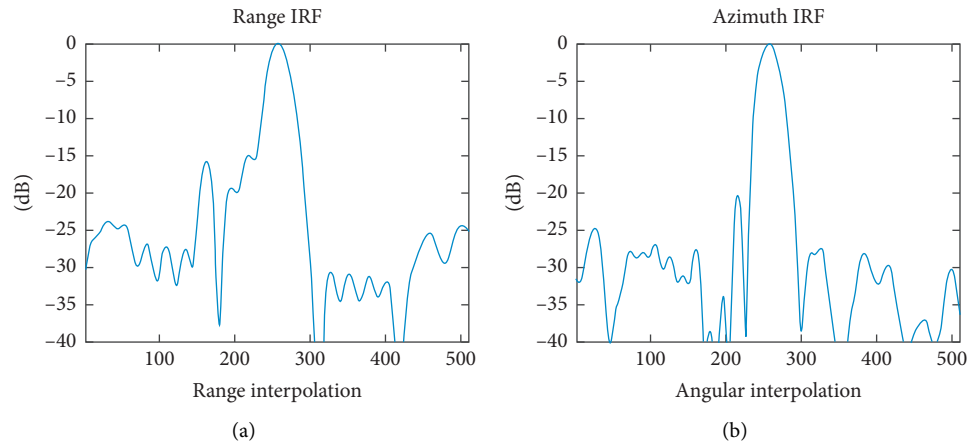


FIGURE 12: Two-dimensional IRFs of the reflector in circle “3”. (a) Range IRF. (b) Azimuth IRF.

results is presented below. The main parameters of the SAR system are tabulated in Table 2. The processed results and estimated motion error are presented in Figure 10. Figure 10(a) is blurred with motion errors and shown in Figure 10(c), while Figure 10(b) shows the SAR image restored by PGA. Magnified images of subscenes A–C in Figure 10 are given in Figure 11 such that the results processed by the proposed method are well-focused. To evaluate the image quality, both range and azimuth IRFs of a single reflector in Scene C is shown in Figure 12, and the peak side lobes of the selected reflector are less than 20 dB.

5. Conclusion

In this paper, we incorporate PGA into the modified FFBP to achieve an accurate autofocus for high-resolution spotlight SAR imaging and investigate its performance in detail. In this method, LOS pseudopolar subimages are reconstructed to provide PGA with a FTR between image domain and its corresponding range-compressed phase history domain. Based on OSF, full-aperture phase error function can be obtained to retrieve the linear phase belonging to each subaperture phase error. Within the recursion of the modified FFBP, phase estimation and correction can be achieved at a high precision and efficiency. It should be noted that the unknown DEM will cause the degradation of the focusing and positioning performance of the method in this paper so that we will study in the future work.

Data Availability

The data used in this article are obtained from a private data source.

Conflicts of Interest

The authors declare that they have no conflicts of interest.

Acknowledgments

This research was funded by National Natural Science Foundation of China (Grant no. 61303031) and the

Fundamental Research Funds for the Central Universities (Grant no. JB181005).

References

- [1] O. Frey, C. Magnard, M. Ruegg, and E. Meier, “Focusing of airborne synthetic aperture radar data from highly nonlinear flight tracks,” *IEEE Transactions on Geoscience and Remote Sensing*, vol. 47, no. 6, pp. 1844–1858, 2009.
- [2] C. V. Jakowatz Jr., N. Doren, and N. Doren, “Comparison of polar formatting and back-projection algorithms for spotlight-mode SAR image formation,” in *Proceedings of the Algorithms for Synthetic Aperture Radar Imagery XIII*, Antalya, Turkey, May 2006.
- [3] F. Yegulalp, “Fast backprojection algorithm for synthetic aperture radar,” in *Proceedings of the IEEE Radar Conference*, pp. 60–65, Waltham, MA, USA, October 1999.
- [4] L. M. H. Ulander, H. Hellsten, and G. Stenstrom, “Synthetic-aperture radar processing using fast factorized back-projection,” *IEEE Transactions on Aerospace and Electronic Systems*, vol. 39, no. 3, pp. 760–776, 2003.
- [5] M. Rodriguez-cassola, P. Prats, G. Krieger, and A. Moreira, “Efficient time-domain image formation with precise topography accommodation for general bistatic SAR configurations,” *IEEE Transactions on Aerospace and Electronic Systems*, vol. 47, no. 4, pp. 2949–2966, 2011.
- [6] M. Zhang, G. Wang, and L. Zhang, “Precise aperture-dependent motion compensation with frequency domain fast back-projection algorithm,” *Sensors*, vol. 17, no. 11, p. 2454, 2017.
- [7] L. Ran, Z. Liu, T. Li, R. Xie, and L. Zhang, “An adaptive fast factorized back-projection algorithm with integrated target detection technique for high-resolution and high-squint spotlight SAR imagery,” *IEEE Journal of Selected Topics in Applied Earth Observations and Remote Sensing*, vol. 11, no. 1, pp. 171–183, 2018.
- [8] H. Cantalloube and C. Nahum, “Motion compensation and autofocus of range/Doppler or bidimensional processing for airborne synthetic aperture radar,” *Aerospace Science and Technology*, vol. 2, no. 4, pp. 251–263, 1998.
- [9] H. Hellsten, J. Torgrimsson, P. Dammert et al., “Evaluation of a geometrical autofocus algorithm within the framework of fast factorized back-projection,” in *IET International Conference on Radar Systems (Radar 2012)*, pp. 1–5, Glasgow, Scotland, October 2012.

- [10] J. N. Ash, "An autofocus method for backprojection imagery in synthetic aperture radar," *IEEE Geoscience and Remote Sensing Letters*, vol. 9, no. 1, pp. 104–108, 2012.
- [11] K. Hu, X. Zhang, S. He et al., "A less-memory and high-efficiency autofocus back projection algorithm for SAR imaging IEEE Geosci," *Remote Sensing Letters*, vol. 12, no. 4, pp. 890–894, 2015.
- [12] L. Chen, D. An, and X. Huang, "Extended autofocus back-projection algorithm for low-frequency SAR imaging," *IEEE Geoscience and Remote Sensing Letters*, vol. 14, no. 8, pp. 1323–1327, 2017.
- [13] J. Wu, Y. Li, W. Pu, Z. Li, and J. Yang, "An effective autofocus method for fast factorized back-projection," *IEEE Transactions on Geoscience and Remote Sensing*, vol. 57, no. 8, pp. 6145–6154, 2019.
- [14] L. Zhang, H.-l. Li, Z.-j. Qiao, M.-d. Xing, and Z. Bao, "Integrating autofocus techniques with fast factorized back-projection for high-resolution spotlight SAR imaging," *IEEE Geoscience and Remote Sensing Letters*, vol. 10, no. 6, pp. 1394–1398, 2013.
- [15] W. G. Carrara, R. S. Goodman, and R. M. Majewski, *Spotlight Synthetic Aperture Radar: Signal Processing Algorithm*, Artech House, Boston, MA, USA, 1995.
- [16] D. E. Wahl, P. H. Eichel, D. C. Ghiglia, and C. V. Jakowatz, "Phase gradient autofocus—a robust tool for high resolution SAR phase correction," *IEEE Transactions on Aerospace and Electronic Systems*, vol. 30, no. 3, pp. 827–835, 1994.
- [17] C. V. Jakowatz and D. E. Wahl, "Considerations for autofocus of spotlight-mode SAR imagery created using a beamforming algorithm," in *Proceedings of the SPIE conference on Algorithms for Synthetic Aperture Radar Imagery XVI*, Orlando, FL, USA, April 2009.
- [18] I. Cumming and F. Wang, *Digital Processing of Synthetic Aperture Radar Data: Algorithm and Implementation*, Artech House, Norwood, MA, USA, 2005.
- [19] K. A. C. Macedo, A. Moreira, and A. Moreira, "An autofocus approach for residual motion errors with application to airborne repeated-pass SAR interferometry," *IEEE Transactions on Geoscience and Remote Sensing*, vol. 46, no. 10, pp. 3151–3162, 2008.
- [20] B. L. Burns and J. T. Cordaro, "A SAR image-formation algorithm that compensates for the spatially-variant effects of antenna motion," in *Proceedings of the SPIE*, pp. 14–24, Orlando, FL, USA, July 1994.
- [21] W. Ye, T. S. Yeo, and Z. Bao, "Weighted least-squares estimation of phase errors for SAR/ISAR autofocus," *IEEE Transactions on Geoscience and Remote Sensing*, vol. 37, no. 5, pp. 2487–2494, 1999.
- [22] G. Wang, M. Zhang, Y. Huang, L. Zhang, and F. Wang, "Robust two-dimensional spatial-variant map-drift algorithm for UAV SAR autofocusing," *Remote Sensing*, vol. 11, no. 3, p. 340, 2019.